

# Design Methodology for Biomimetic Propulsion of Miniature Swimming Robots

**Bahareh Behkam**

**Mechanical Engineering Department**

**5000 Forbes Ave**

**Carnegie Mellon University**

**Pittsburgh, PA 15213**

**Ph: 412-268-8847**

**Fax: 412-268-3348**

**behkam@cmu.edu**

**Metin Sitti**

**Mechanical Engineering Department**

**5000 Forbes Ave**

**Carnegie Mellon University**

**Pittsburgh, PA 15213**

**Ph: 412-268-3632**

**Fax: 412-268-3348**

**sitti@cmu.edu**

## **Abstract**

Miniature and energy efficient propulsion systems hold the key to maturing the technology of swimming microrobots. In this paper, two new methods of propulsion inspired by the motility mechanism of prokaryotic and eukaryotic microorganisms are proposed. Hydrodynamic models for each of the two methods are developed and the optimized design parameters for each of the two propulsion modes are demonstrated. To validate the theoretical result for the prokaryotic flagellar motion, a scaled up prototype of the robot is fabricated and tested in silicone oil using the Buckingham PI theorem for scaling. The proposed propulsion methods are appropriate for the swimming robots which are intended to swim in low velocity fluids.

*Keywords*—**Microrobotics, biomimetic robotics, prokaryotic flagellar motion, eukaryotic flagellar motion.**

**[Final version of paper can be found in ASME Journal of Dynamic Systems and Measurement Control]**

## **I. INTRODUCTION**

One of the primary goals of medical microrobots is to reach currently inaccessible areas of the human body and carry out a host of complex operations such as minimally invasive surgery (MIS), highly localized drug delivery, and screening for diseases at their very early stages. Miniature swimming robots could be greatly beneficial for screening and treatment of many diseases at their early stages. Due to their small size, swimming microrobots possess very small Reynolds ( $Re$ )

numbers. Reynolds number is defined as the ratio of inertial forces to viscous forces and characterizes fluid flow. A low Reynolds number infers that the inertial forces are less significant or even negligible compared to the viscous forces. Therefore, microscale swimmers in general experience drastically different hydrodynamics compared to their macroscale counterparts. There are few biomimetic swimming robots, mostly fin-driven, developed [1-5]. Since fish-like biomimetic robots rely on inertial forces for propulsion, miniaturization will make them ineffective [1]. In another design, introduced by Ishiyama *et al.* [5], an external magnetic field is used to rotate a small ferromagnetic screw within the liquid. The main advantage of this untethered machine is that it does not require onboard power source or controller. It has been demonstrated that this spiral machine can swim in liquids of various viscosities in a broad range of  $Re$  numbers. However, speed limitation is the main deficiency of this machine. For frequencies higher than the frequency which corresponds to the maximum acquirable speed, the rotation of the machine could not synchronize with the rotational frequency of the external field hence the velocity decreases.

Here, we propose novel, safe, miniature and energy efficient biomimetic propulsion concepts, inspired by prokaryotic flagellar motion and eukaryotic flagellar motion. The peritrichous flagellation used by prokaryotic microorganisms (bacteria) such as *E. Coli* and *S. Marcescens* [6-7], is depicted in Fig. 1. The flagella of these cells are randomly distributed over the cell surface and each flagellar motor rotates independently of the others. Hydrodynamic interactions among flagella cause them to coordinate, coalesce and bundle behind the cell during swimming [8]. The flagellum is a propulsive organelle that includes a reversible rotary motor embedded in the cell wall, and a filament that extends into the external medium [9]. The filament is a long ( $\sim 10 \mu\text{m}$ ), thin ( $\sim 20 \text{ nm}$ ) helix ( $2.5 \mu\text{m}$  pitch,  $0.5 \mu\text{m}$  diameter) that rotates at speed of  $\sim 100 \text{ Hz}$  [10]. Flagellation of eukaryotic microorganism such as spermatozoa is shown in Fig. 2. Eukaryotic flagella are morphologically and mechanically different from prokaryotic flagella. Eukaryotic flagella are usually larger and have more flexible structures. They function by bending contrary to prokaryotic flagella which function by rotating. For both of these microorganisms  $Re \sim 10^{-6} - 10^{-4}$ , thus signifying the dominance of viscous effects over inertial effects. In both cases thrust force arises from viscous shearing. Therefore, these propulsion methods can perform effectively even at very small scales and low  $Re$  numbers. From here on, we refer to prokaryotic flagellar motion and eukaryotic flagellar motion, as helical wave propulsion and planar wave propulsion, respectively.

This research work intends to investigate the potential of using helical and planar wave for microrobotic propulsion. By spinning a rigid helical structure at low Reynolds numbers, a thrust force should be observed that can be used for propelling a microscale swimming robot. Schematic of such a robot is depicted in Fig. 3. Increasing the number of these rigid helical structures aka flagella to an optimum number enhances the performance of the robot. Alternatively, swimming microrobots could utilize one or several undulating propulsive elements resembling the eukaryotic flagella. Schematic of the

swimming robot propelled by planar wave is shown in Fig. 6. In this work, a comparison between these two propulsion methods is presented. In the case of helical wave propulsion, the analytical model is validated by experimental measurement of the thrust force. The proposed methods are appropriate for the swimming robots intended to swim in stationary or low velocity biofluids. Potential targeted medical applications for these robots include screening for diseases at their early stages and eventually MIS and localized drug delivery in the urinary system, eyeball cavity, and cerebrospinal fluid.

## II. METHODOLOGY

The first step towards developing an effective propulsion system is to understand the hydrodynamics of the miniature swimming robots. Based upon the application that the miniature medical robot is designed for, the body of the robot can have a diameter ranging from about few micrometers to few millimeters. Assuming the biofluid media that the robot swims in to have the hydrodynamic properties of water,  $Re$  number for miniature swimming robot will vary within the range of  $10^{-4}$ -100. Therefore, either the  $Re$  of the miniature robot or local  $Re$  of its propulsive components would be much smaller than 1.

## III. MODELING

### A. Low Reynolds Number Flow

Reynolds number is defined as:

$$Re = \frac{\rho V l}{\mu} \quad (1)$$

where  $\rho$  and  $\mu$  are density and dynamic viscosity of the fluid, respectively.  $V$  is the velocity of the object relative to the flow and  $l$  is the characteristic dimension of the object. For most microscale objects moving in water,  $Re \ll 1$  due to the size and velocity of the object and fluid properties of water. Such flows are often characterized as *stokes flow*. For this type of flow the inertia terms in Navier-Stokes equation are dropped and the equation reduces to

$$\nabla p + \mu \nabla^2 V = 0 \quad (2)$$

where  $p$  is the pressure. This equation is absent of any time dependent terms, signifying that the generated propulsion force only depends on the propeller's relative position not timing during a cycle. This infers that any motion completely retracing its own steps, like the flapping of fish's fin, will result in no net forward movement. The classic example is the motion of scallop, also known as scallop theorem. A scallop propels forward by slowly opening its hinge and then quickly closing it. The water squirts out and pushes the scallop forward. If scallop were scaled down to be a few micrometers, this motion would result in periodic slight forward and backward motion with no net displacement.

To overcome this problem, organisms living in the realm of low Reynolds number either have propulsive organelles with nonsuperimposable mirror image (*e.g.* helical wave propulsion) or their propulsive organelles assume different geometries throughout the cycle (*e.g.* planar wave propulsion). An example of the former case is helical wave propulsion and traveling planar wave propulsion is an example of the latter case.

### B. Modeling of the Helical Wave Propulsion

We intend to develop a model which takes the dimensions and rotational frequency of the helix as the inputs and returns important performance parameters such as propulsion force ( $F_x$ ), forward velocity ( $V_x$ ), and generated torque ( $M_x$ ). The analysis is performed in cylindrical coordinates. The schematic of the robot along with the system of coordinates and forces applied on the tail are shown in Fig. 3. As stated before, inertial forces at this scale are insignificant, hence the equations for conservation of linear and angular momentum in  $x$ -direction can be written as:

$$\sum F_{x,tail} - F_{head} = 0 \quad (3)$$

$$\sum M_{x,tail} - M_{head} = 0 \quad (4)$$

For an element  $ds$  on the helix, the propulsive force in  $x$ -direction in terms of its normal and longitudinal components is:

$$dF_x = dF_n \sin \beta - dF_l \cos \beta \quad (5)$$

and the force in  $\theta$ -direction is equal to:

$$dF_\theta = -(dF_n \cos \beta + dF_l \sin \beta) \quad (6)$$

which results in a torque about  $x$ -axis,

$$dM_x = A_{helix} dF_\theta = -A_{helix} (dF_n \cos \beta + dF_l \sin \beta) \quad (7)$$

where  $A$  is the amplitude of the helix and  $\beta$  is the constant pitch-angle between the helix and the  $x$ -axis,

$$\tan \beta = \frac{2\pi}{\lambda_{helix}} A_{helix} \quad (8)$$

in which  $\lambda$  is the wavelength of the helix. As stated in Eq. (4), for the resultant torque applied on the robot to be zero, the head of the robot has to rotate. Therefore, in a coordinate system fixed with respect to the fluid at large distance the resulting motion of the robot is one in which every cross section of the tail rotates at  $\omega_{app} = \omega - \Omega$  in  $\theta$ -direction and the head rotates in the opposite direction with the angular velocity of  $\Omega$ . There would be an additional viscous torque acting on

element  $ds$  of the tail which results from the fluid reaction on the element of the tail which rotates about the tangent of its central curve at the velocity of  $\Omega_s = \Omega \cos\beta$ . The  $x$ -component of this torque is [11]:

$$dL_{tail} = dM_s \cos\beta = 4\pi\mu d_{helix}^2 \Omega \cos\beta dx \quad (9)$$

where  $d$  is half the thickness of the tail filament.

Hancock [12] developed very useful relationships for calculating the normal and tangential coefficients of viscous resistance acting on the surface of a long thin cylindrical filament moving through a viscous fluid. This is known as *Resistive Force Theory* (RFT). It states that the tangential and normal forces acting on a cylindrical element of length  $ds$ , respectively are:

$$dF_n = -C_{n,helix} V_n ds \quad (10)$$

$$dF_l = -C_{l,helix} V_l ds \quad (11)$$

where  $V_n$  and  $V_l$  are the normal and tangential velocities of the element and  $C_{n,helix}$  and  $C_{l,helix}$  are the corresponding coefficients of resistance driven empirically by Gray and Hancock [13] for a flagellum with both free ends:

$$C_{n,helix} = \frac{4\pi\mu}{\ln\left(\frac{2\lambda_{helix}}{d_{helix}}\right) + \frac{1}{2}} \quad (12)$$

$$C_{l,helix} = \frac{2\pi\mu}{\ln\left(\frac{2\lambda_{helix}}{d_{helix}}\right) - \frac{1}{2}} \quad (13)$$

Therefore,

$$dF_n = C_{n,helix} (V_\theta \cos\beta - U \sin\beta) \sec\beta dx \quad (14)$$

$$dF_l = C_{l,helix} (V_\theta \sin\beta + U \cos\beta) \sec\beta dx \quad (15)$$

where  $V_\theta = A_{helix} \omega_{app} = A_{helix} (\omega - \Omega)$ . Equations (3) and (4) can now be rewritten as

$$\int_0^{n\lambda} dF_x - F_{head} = 0 \quad (16)$$

$$\int_0^{n\lambda} (dM_x + dL_{tail}) + M_{head} = 0 \quad (17)$$

If the head of the robot is modeled as a sphere,  $F_{head}$  and  $M_{head}$  are calculated as:

$$F_{head} = 6\pi\mu a U \quad (18)$$

$$M_{head} = 8\pi\mu a^3 \Omega \quad (19)$$

where  $a$  is the radius of the head. Substituting Eq. (5), (8), (14), (15) and Eq. (18) in (16) and Eq. (7), (8), (9), (14), (15), and (19) in Eq. (17) yields two simultaneous equations that can be solved for  $U$  and  $\Omega$  :

$$U = n\lambda_{helix} V_{\theta} \sin\beta \cos\beta \frac{C_{n,helix} - C_{l,helix}}{n\lambda(C_{n,helix} \sin^2\beta + C_{l,helix} - C_{l,helix} \sin^2\beta) + 6\pi\mu a \cos\beta} \quad (20)$$

$$\Omega = \frac{n\lambda_{helix} \left( -6\pi\mu a h_{helix} V_{\theta} (\sin^2\beta \cos\beta (C_{l,helix} + C_{n,helix}) + C_{n,helix} \cos\beta) - n\lambda_{helix} h_{helix} V_{\theta} C_{n,helix} C_{l,helix} \right)}{8\pi\mu a^3 (6\pi\mu a (1 - \sin^2\beta) + n\lambda_{helix} \cos\beta (C_{n,helix} \sin^2\beta - C_{l,helix} \sin^2\beta + C_{l,helix}))} \quad (21)$$

$$+ \frac{n\lambda_{helix} (6\pi\mu a L_{tail} (1 - \sin^2\beta) + n\lambda_{helix} L_{tail} (\sin^2\beta \cos\beta (C_{n,helix} - C_{l,helix}) + C_{l,helix} \cos\beta))}{8\pi\mu a^3 (6\pi\mu a (1 - \sin^2\beta) + n\lambda_{helix} \cos\beta (C_{n,helix} \sin^2\beta - C_{l,helix} \sin^2\beta + C_{l,helix}))}$$

The efficiency of the robot can be defined as

$$\eta = \frac{F_x \cdot U}{M \cdot \omega} \quad (22)$$

A non-dimensional analysis [14] of the force, torque and velocity of the system shows that

$$\frac{M}{\mu\omega L^2} = f_M \left( \frac{A}{L}, \frac{a}{L}, \frac{\lambda}{L}, \frac{d}{L} \right) \quad (23)$$

$$\frac{F_x}{\mu\omega L^2} = f_{F_x} \left( \frac{A}{L}, \frac{a}{L}, \frac{\lambda}{L}, \frac{d}{L} \right) \quad (24)$$

$$\frac{U}{L\omega} = f_U \left( \frac{A}{L}, \frac{a}{L}, \frac{\lambda}{L}, \frac{d}{L} \right) \quad (25)$$

From Eq. (23) through Eq. (25), one can conclude that both efficiency and velocity are functions of geometry only. An optimum design is one which yields the maximum efficiency and velocity. Figure 4 and 5 show how velocity and efficiency change as functions of the independent geometrical parameters. These graphs can be used for determining the dimensions of the helix which yield the highest velocity and efficiency, considering the geometrical constraints pertaining to the specific application the robot is designed for. An increase in the tail filament diameter will increase both velocity and efficiency. However, the diameter should be small enough for the slender body assumption to hold. A decrease in the size of the body of the robot will also result in increase of both velocity and efficiency. The only constraints on the size of the body are the microscale manufacturing-assembly issues and the size of the components that need to be installed within the body of the robot. As for the amplitude of the helix, the larger amplitude results in a higher velocity but lower efficiency, where it can be seen that the rate of the decrease of the efficiency is much higher than the rate of the increase of the velocity. Hence it is a trade off which one needs to decide whether a higher velocity of a higher efficiency is of interest for the specific application.

### C. Modeling of the Planar Wave Propulsion

Similar to the analysis presented for helical wave propulsion, the viscous forces exerted on the tail in  $x$  and  $y$  directions can be decomposed in their normal and lateral components. For such undulatory systems, the retarding effect of the tangential forces is compensated by propulsive component of the viscous forces exerted in normal direction on the surface. Gray and Hancock [15] analyzed the propulsion of sea-urchin spermatozoa and demonstrated analytical relationships for the force exerted on the tail by the surrounding medium and also the propulsion speed of the spermatozoon as a function of form and speed of the propagation of the bending wave generated by the tail.

If the wave generated by the tail conforms to a sine curve, it can be written as:

$$y = h_{planar} \sin\left(\frac{2\pi}{\lambda_{planar}}(x + V_w t)\right) \quad (26)$$

where  $h$  is the amplitude of the wave,  $\lambda$  is the wavelength of the wave,  $V_w$  is the wave speed. Forward thrust force exerted by each complete wave at any instant of time is calculated as:

$$F_{xx} = \int_0^{\lambda_{planar}} dF_{xx} = \frac{2\pi^2 h_{planar}^2 V_w (C_{n,planar} - C_{l,planar})}{\lambda_{planar}} C_{l,planar} \lambda_{planar} V_x \quad (27)$$

and the total thrust force generated by the tail is

$$F_x = n F_{xx} \quad (28)$$

where  $n$  is number of waves in the tail,  $V_x$  is the linear velocity of the system,  $C_{l,planar}$  and  $C_{n,planar}$  are the coefficients of resistance in longitudinal and normal directions, respectively and are equal to

$$C_{l,planar} = \frac{2\pi\mu}{\ln\left(\frac{d_{planar}}{2\lambda_{planar}}\right) + \frac{1}{2}} \quad (29)$$

$$C_{n,planar} = 2C_{l,planar} \quad (30)$$

The viscous forces in normal direction for the length  $x$  of the flagellum at any instant of time is

$$F_{yy} = h_{planar} \sin\left(\frac{2\pi x}{\lambda_{planar}}\right) (V_x (C_{l,planar} - C_{n,planar}) - V_w C_{n,planar}) \quad (31)$$

and the total normal viscous force is

$$F_y = n \int_0^{\lambda_{planar}} F_{yy} dx \quad (32)$$

Since there is no net motion of the system in  $y$  direction, sum of the forces in  $y$  direction for a complete wave is equal to zero.

For a system with spherical head, the forward velocity is

$$V_x = \frac{2f\pi^2 b_{planar}^2}{\lambda_{planar}} \left\{ \frac{1}{1 + \frac{4\pi^2 b_{planar}^2}{\lambda_{planar}^2} - \left(1 + \frac{2\pi^2 b_{planar}^2}{\lambda_{planar}^2}\right)^{1/2}} \frac{3a}{n\lambda_{planar}} \left[ \log \frac{d_{planar}}{2\lambda_{planar}} + 1 \right]} \right\} \quad (33)$$

where  $f$  is frequency of the wave. The velocity of the tail in  $y$  direction is

$$V_y = \frac{dy}{dt} = \frac{2\pi h_{planar}}{\lambda_{planar}} \cos \frac{2\pi}{\lambda_{planar}} (x + V_w t) \quad (34)$$

The efficiency of the robot can now be defined as

$$\eta = \frac{F_x V_x}{F_x V_x + F_y V_y} \quad (35)$$

A non-dimensional analysis [14] of the force and velocity of the system shows that:

$$\frac{F_x}{\mu f} = g_1 \left( \frac{h_{planar}}{L}, \frac{a}{L}, \frac{\lambda_{planar}}{L}, \frac{d_{planar}}{L} \right) \quad (36)$$

$$\frac{V_x}{Lf} = g_2 \left( \frac{h_{planar}}{L}, \frac{a}{L}, \frac{\lambda_{planar}}{L}, \frac{d_{planar}}{L} \right) \quad (37)$$

Equations (36) and (37) show that both efficiency and velocity are only functions of geometry. Similar to the helical wave propulsion, an optimum design is one which yields the maximum efficiency and velocity. Figures 6 and 7 show how velocity and efficiency change with independent geometrical parameters. An increase in the amplitude of propulsive component will result in increase in both velocity and efficiency. The maximum magnitude of the amplitude is determined by (a) The maximum allowable diameter of the robot and (b) The ratio of the amplitude to the wave length. This ratio has to be kept small for the theoretical model to be valid. Similar to helical wave propulsion, an increase in the thickness of the filament will yield increase in velocity and efficiency. The only limit is that the slender body theory should always be satisfied. Decrement of the size of the body of the robot will cause rapid rise of both velocity and efficiency. As explained in §III.B, the only constraints in miniaturizing the body are the available micro-manufacturing and assembly technology and the size of the already developed components which will be installed in the body of the robot.



#### IV. EXPERIMENTS

To examine the validity of the developed model, the thrust force in the case of helical wave propulsion, at Reynolds numbers smaller than 1, is measured experimentally. To simplify the fabrication and characterization process, the dimensions of the prototype are scaled up according to the Buckingham PI theorem and the experiment is carried out in silicone oil which has a higher viscosity than water. This way the  $Re$  number of the scaled up prototype is identical to the  $Re$  number of the microscale robot to be developed in near future. According to Buckingham PI theorem, the ratio of  $F/(\mu\omega L^2)$  is the same for the scaled up prototype and the microscale robot.

Schematic of the experimental set up is shown in Fig. 9. The body of the prototype is a two-phase stepper motor from Faulhaber<sup>®</sup>. This motor is 14.5 mm in diameter and 16.5 mm in length. The helix is made from steel wire and is coupled with the motor using a Delrin coupler. The experiment was performed for 3 different geometries of flagella. The dimensions are given in Table 1. In each case, the prototype was perpendicularly mounted to a thin steel cantilever beam which is 14 cm long with a cross section of 19.05 by 0.78 mm<sup>2</sup>. The assembly was submerged in silicone oil with viscosity of 350 cSt from Dow Corning<sup>®</sup>. The silicone oil container was 22.2 cm long, 21.11 cm wide and 17.63 cm deep. The motor was run in a range of frequencies from 4 Hz to 7 Hz with a step of 0.5 Hz. There were two constraints determining the range of the frequencies: (1) If the frequency was too low, the beam deflection caused by the propulsion force would be too small to be measured by the laser micrometer (2) If the frequency was too high, the stepper motor wouldn't be able to generate enough torque required for the rotation of the flagella. Thrust force generated by the system deflected the beam it was attached to. A laser micrometer (LS-3100, Keyence Inc.) measures the deflection of the calibrated beam due to the thrust force. Recorded deflection data were passed through a Butterworth filter to eliminate the noise. Deflection data was then used to calculate the thrust force.

Table 1: Dimensions of the helical tail of the scaled-up prototype

<b>Dimensions (mm)</b>	<b>Design I</b>	<b>Design II</b>	<b>Design III</b>
Filament thickness, $2d$	0.43	0.63	0.43
Amplitude, $A$	0.8	1.6	1.6
Wavelength, $\lambda$	5	5	12
Length, $L$	50	50	50

Figure 10 depicts the experimental results for the thrust force generated by the helical wave propulsion of the prototype in silicon oil. As predicted by theory, the experimental values of the force vary linearly with the frequency; however, for Design I and Design III the experimental results are larger than the predicted theoretical values. This seems to

be largely due to the wall effect. It should be noted that the helical wave propulsion model in §III was developed with the assumption that there is no wall effect meaning the walls are far enough so that they will not significantly affect the fluid flow. At low  $Re$ , the body influences the fluid flow at greater lateral distances from its outer surface. It is shown [16] that below  $Re = 1$ , for the wall to have negligible effect it has to be  $y > (20l / Re)$  distance away from the body in which  $l$  is the characteristic length of the body. For the experiments performed on Design I and III, the distance from the wall was not large enough to be ignored; the effect is shown as an increase in the values of thrust force when compared to the theoretical predictions. To confirm our hypothesis, we performed the experiment for Design III in two containers of different size. As shown in Fig. 10, for the larger container the wall effect has decreased and the values are getting closer to the theoretical predictions. For Design II the condition of  $y > (20l / Re)$  is satisfied and wall effect is negligible hence the experiment and theory are in close agreement. Authors are currently working on implementing the wall effect into the model. It is shown that the wall effect can be accounted for by redefining the resistance coefficients [17] as  $C^*$  :

$$\frac{C^*}{C} = \left( 1 - z \frac{C}{3\pi\mu} \frac{l}{h} \right)^{-1} \quad (38)$$

where  $C$  is the coefficient of resistance in the absence of the boundary and  $z$  is a function of the geometry and the direction of the motion. Another factor contributing to the difference between the theory and experiment is the fact that coefficients presented in Eq. (12) and (13) are for a flagellum with both free ends. The body attached to one end of the flagellum modifies the fluid flow field experienced by the flagellum. This interaction is not considered in RFT. This is probably insignificant for small bodies but for large bodies such as the one used in this experiment, the use of a more accurate slender-body theory will yield a more accurate result [13].

The uncertainty in the experimental data is due to (a) The uncertainties associated with the measurement equipment and the user, (b) The uncertainty of the calibration process.

The models developed here are valid for  $Re \ll 1$  therefore they would be valid for analyzing any swimming robot regardless of the size as long as the condition of  $Re \ll 1$  is satisfied. Also our scaled up prototype is geometrically, kinematically and dynamically similar to the miniature robot to be developed hence the results from the experiment should be identical to the results we would get from the testing of the miniature robot. The only issue is the wall effect changes with both  $Re$  and the characteristic length and becomes smaller for smaller robots. So if we were to do the experiment for a microscale robot in exact same container with water, we would get different results just because of the wall effect which exist on the scaled-up prototype. Also as we approach microscale, it is most likely that the tail of the robot would become more compliant and elasticity of the tail and the effect of neighboring elements need to be included in the model.

## V. CONCLUSION

Biomimetic propulsion mechanisms inspired by prokaryotic and eukaryotic microorganisms were introduced. Analytical models were developed to predict the values for thrust force, required torque, velocity, and efficiency. It is shown that all the aforementioned parameters are functions of geometry only. Applying Buckingham PI theorem a scaled-up prototype of the robot was constructed and tested in silicone oil. Experimental results for thrust force are shown to be in agreement with theoretical values predicted by the RFT model. Increasing the number of flagella will enhance the speed and perhaps the efficiency of the swimming robot. The optimum design of a multi-flagella system in terms of number of flagella and spacing is being investigated. Another common method of propulsion among microorganisms is eukaryotic flagellation. Eukaryotic flagella actively change their shape in an undulatory fashion. Analytical model of the hydrodynamics of eukaryotic flagellation is presented here. Assuming a 100% efficiency for the actuators used for generation of both helical and planar wave, it is shown that planar wave propulsion has a higher efficiency and results in a significantly higher linear velocity. However, in reality actuators have very different efficiencies. Some, such as piezoelectric actuators are very efficient while others such as polymer actuators have low efficiencies. For a fair and practical comparison of overall efficiencies of the two modes of propulsion, the efficiency of the selected actuator has to be included in calculating the overall efficiency.

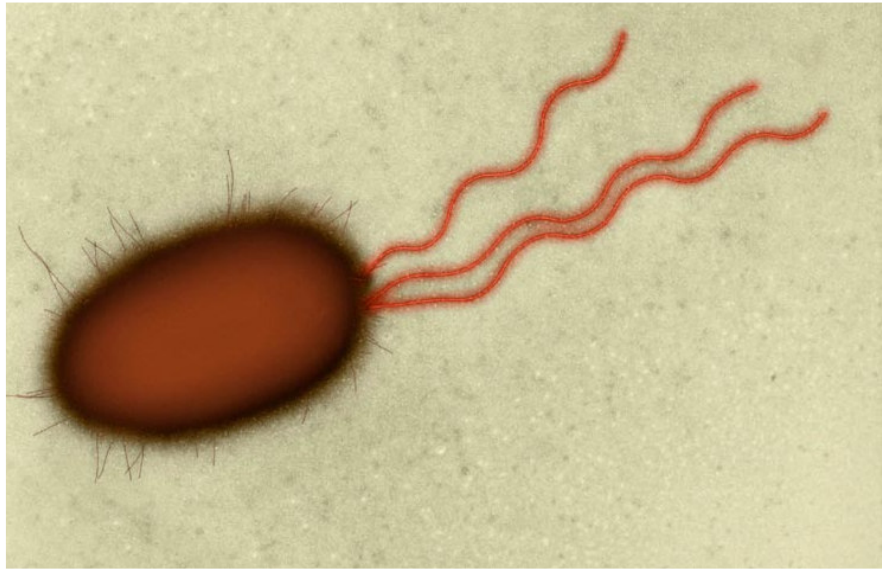
## ACKNOWLEDGMENTS

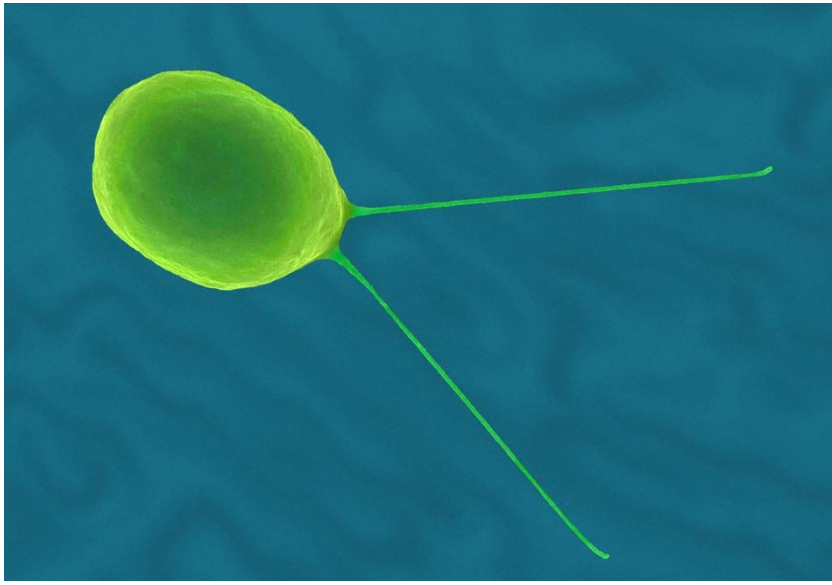
This work is supported in part by ICES-DOWD fellowship. Authors' special gratitude goes to Shelley Anna and Ender Finol at Carnegie Mellon University for stimulating discussions. We also appreciate Eddie Lu's help in conducting the experimental measurements.

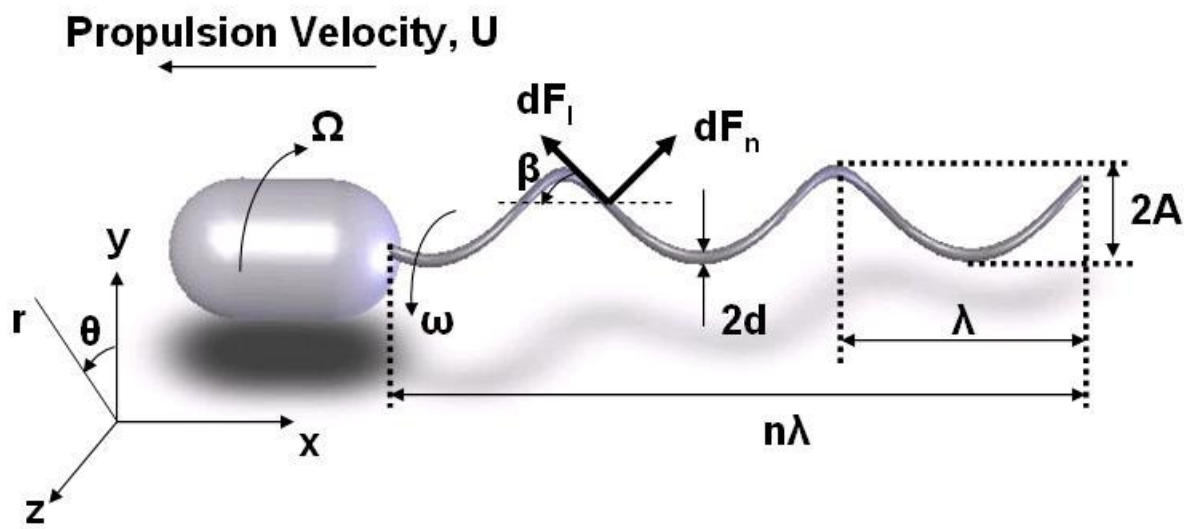
## REFERENCES

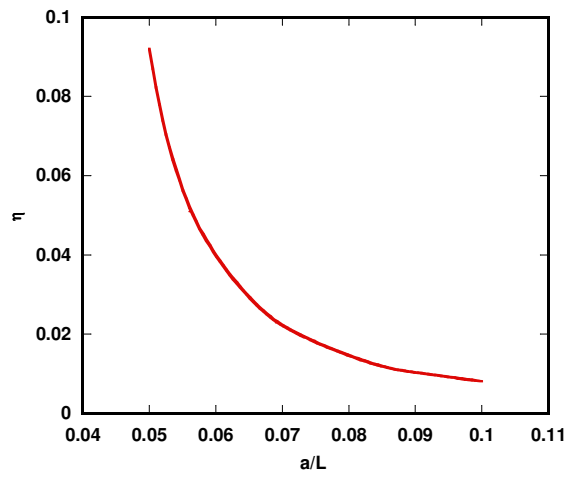
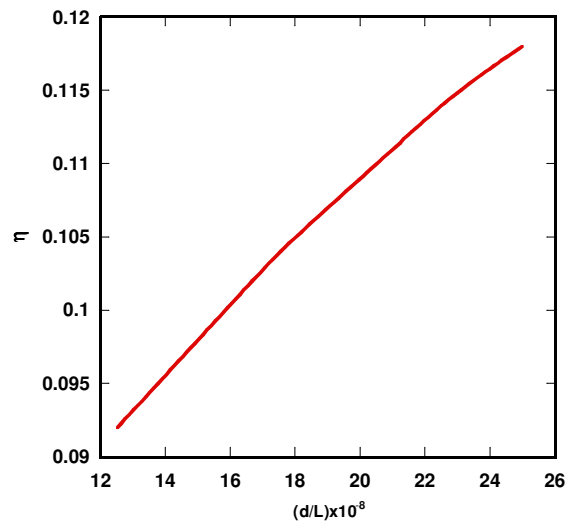
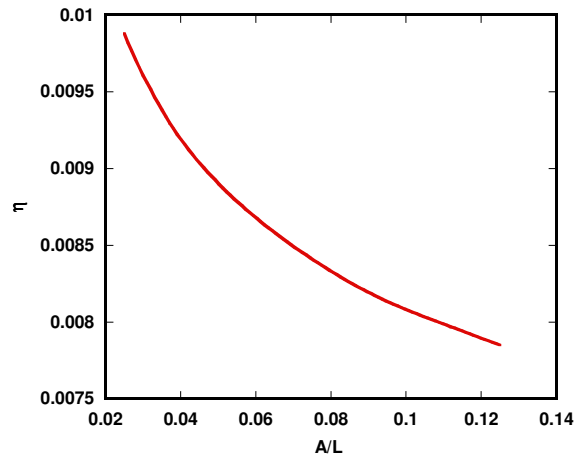
- [1] Fukuda, T., Kawamoto, A., Arai, F., and Matsuura, H., 1994, "Mechanism and Swimming Experiment of Micro Mobile Robot in Water," *Proc. of IEEE International Workshop on Micro Electro Mechanical Systems (MEMS'94)*, pp.273-278.
- [2] Guo, S., Hasegaw, Y., Fukuda, T., and Asaka, K., 2001, "Fish -Like Underwater Microrobot with Multi DOF," *Proceedings of 200 International Symposium on Micromechatronics and Human Science*, pp. 63-68.
- [3] Jung, J., Kim, B., Tak, Y., and Park, J., 2003, "Undulatory Tadpole Robot (TadRob) Using Ionic Polymer Metal Composite (IMPC) Actuator," *Proceedings of the 2003 IEEE International Conference on Intelligent Robots and Systems*, pp. 2133-2138.
- [4] Zhang, Y., Wang, Q., Zhang, P., Wang, X., and Mei, T., 2004, "Dynamic Analysis and Experiment of a 3mm Swimming Microrobot," *Proceedings of the 2004 IEEE International Conference on Intelligent Robots and Systems*, pp. 1746-1750.
- [5] Honda, T., Arai, K., and Ishiyama, K., 1999, "Effect of Micro Machine Shape on Swimming Properties of the Spiral-Type Magnetic Micro-Machine," *IEEE transaction on magnetics*, **35**, pp. 3688-3690.

- [6] Behkam, B. and Sitti, M., 2004 “*E. Coli* Inspired Propulsion for Swimming Microrobots,” IMECE2004-59621, *Proceedings of 2004 ASME International Mechanical Engineering Conference and Exposition*.
- [7] Edd, J., Payen, S., Rubinsky, B., Stoller, M.L., and Sitti, M., 2003, “Biomimetic Propulsion for a Swimming Surgical Microrobot,” *Proceedings of the 2004 IEEE International Conference on Intelligent Robots and System*, pp. 2583-2588.
- [8] Darnton, N., Turner, L., Breuer, K., and Berg, H., “Moving Fluid with Bacterial Carpets,” *Biophysical Journal*, **86**, pp. 1863-1870, March 2004.
- [9] Berg, H., 2003, “The Rotary Motor of Bacterial Flagella,” *Annual Review of Biochemistry*, **72**, pp. 19-54,
- [10] Leifson, E., 1960 “Atlas of Bacterial Flagellation,” *Academic Press, New York and London*.
- [11] Chwang, T. and Wu. T., 1971 “A Note on the Helical Movement of Microorganisms,” *Proceedings of Royal Society of London, B*, **178**, pp. 327-346.
- [12] Hancock, G., 1953, “The Self-Propulsion of Microscopic Organisms through Liquids,” *Proceedings of Royal Society of London, A*, **217**, pp. 96-121.
- [13] Johnson, R.E. and Brokaw, C. J., 1979, “Flagellar Hydrodynamics: A Comparison between Resistive-Force Theory and Slender-Body Theory,” *Biophysics Journal*, **125**, pp. 113-127.
- [14] Fox, R., McDonald, A., and Pritchard, P., 2004, “Introduction to Fluid Mechanics,” John Wiley & Sons, pp. 273-300.
- [15] Gray, J. and Hancock, G., 1955, “The Propulsion of Sea-Urchin Spermatozoa,” *Journal of Experimental Biology*, **32**, pp. 802-814.
- [16] Vogel, S., 2003, “Comparative Biomechanics: Life’s Physical World,” Princeton University Press, pp. 227-244.
- [17] Brennen, C. and Winet, H., 1977, “Fluid Mechanics of Propulsion by Cilia and Flagella,” *Annual Review of Fluid Mechanics*, **9**, pp. 339-398.

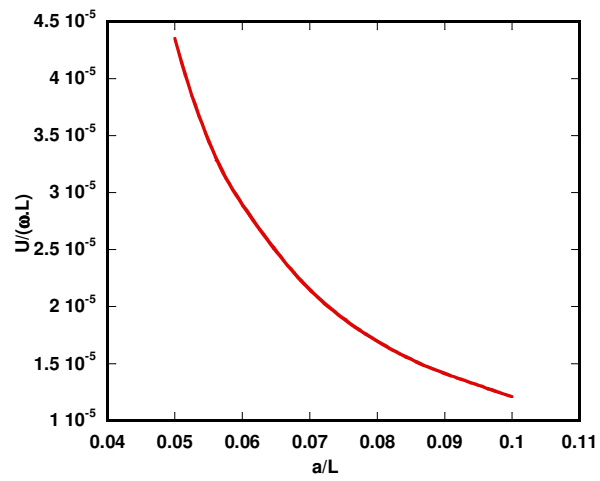
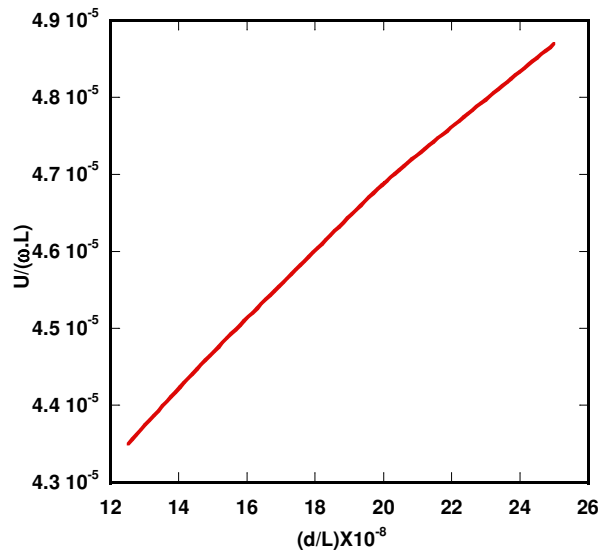
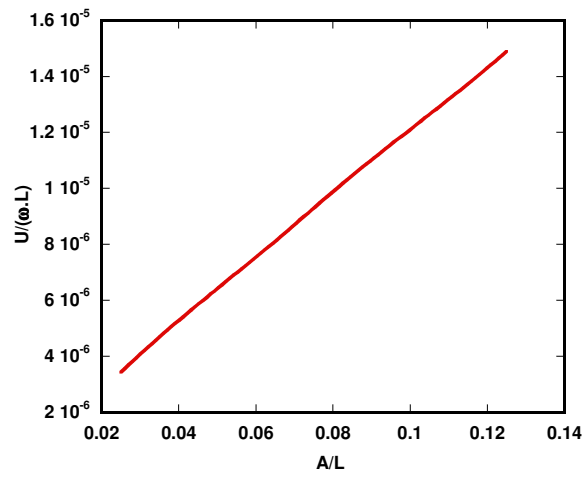


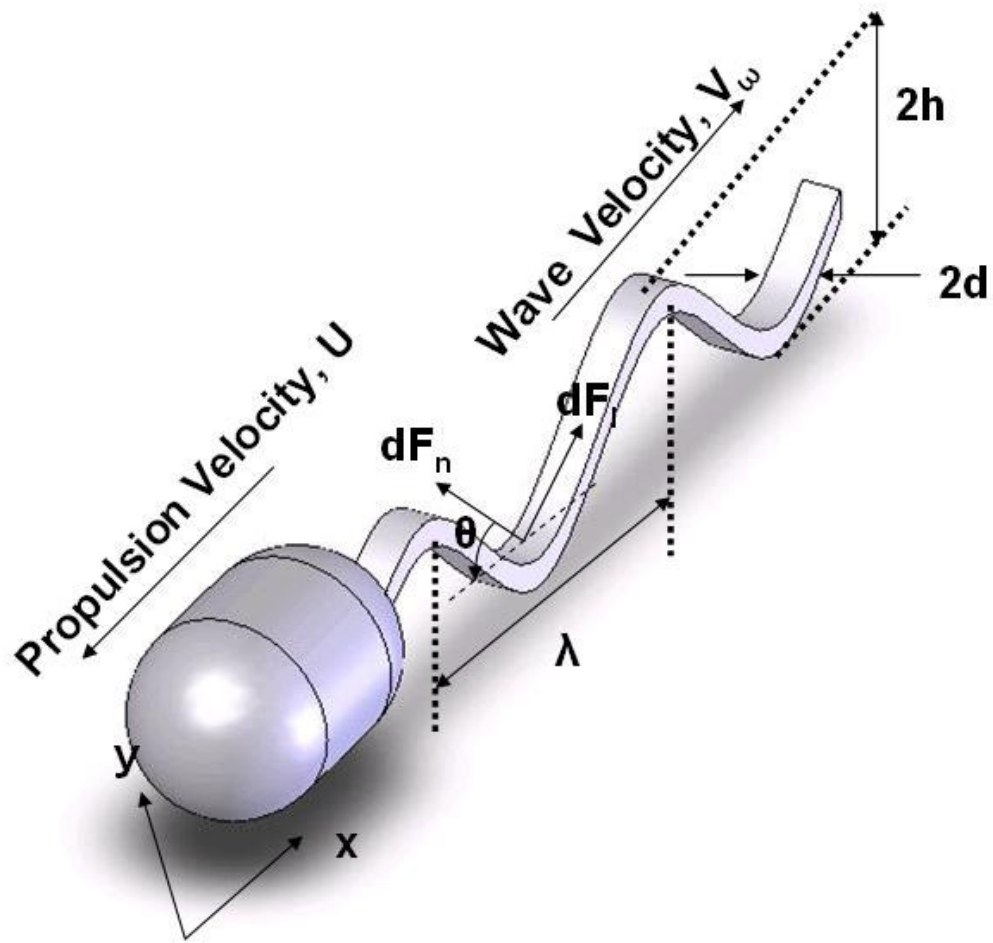


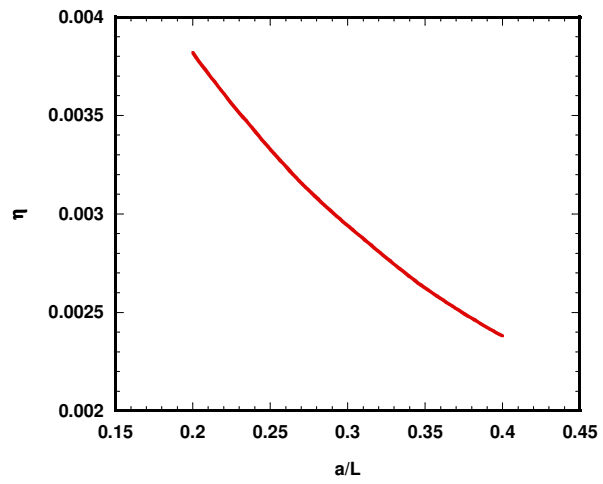
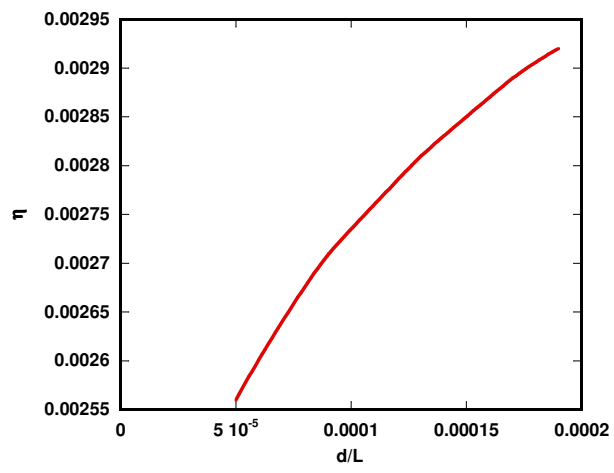
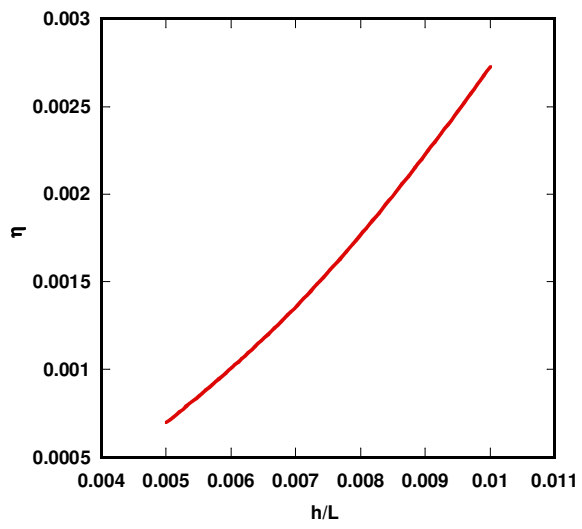


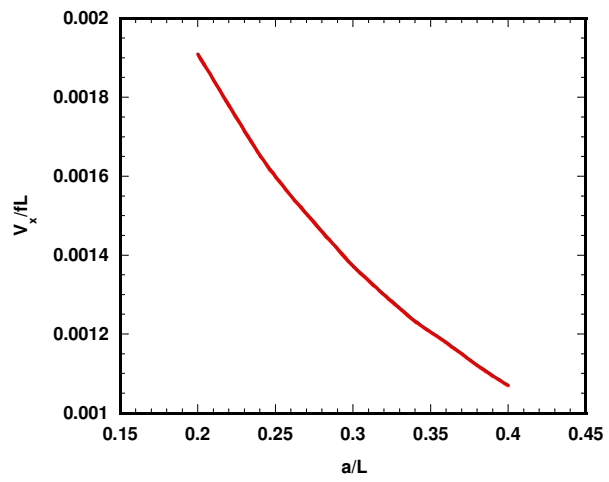
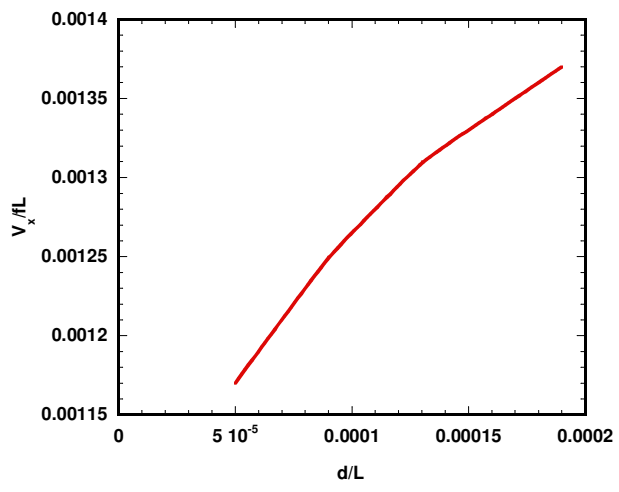
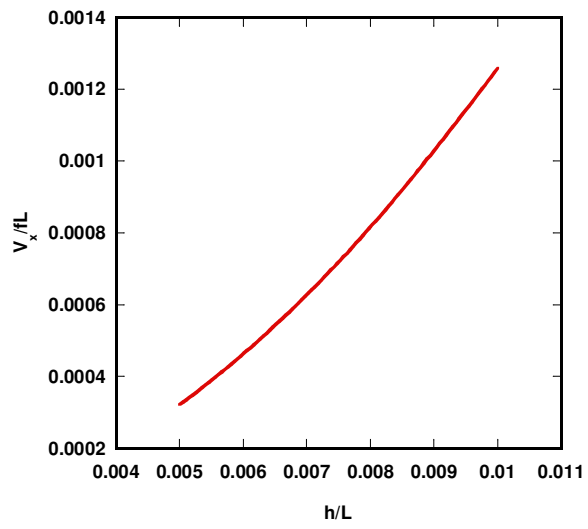


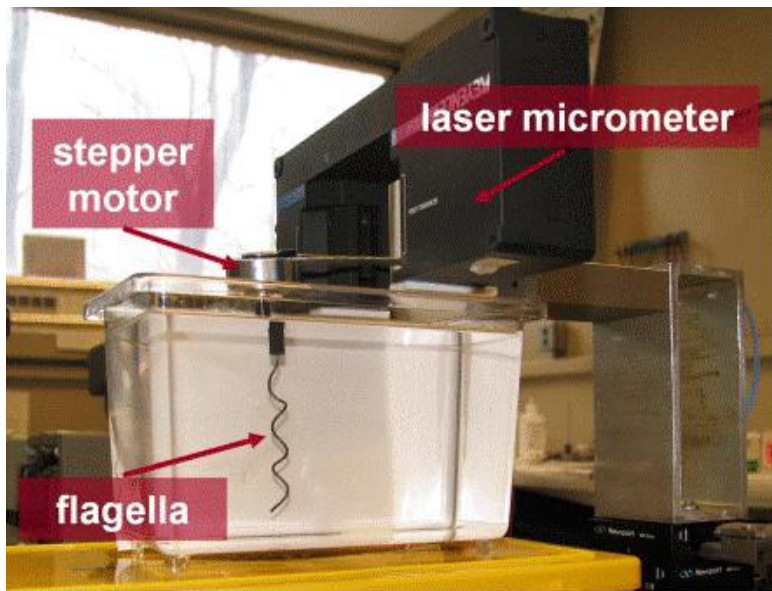


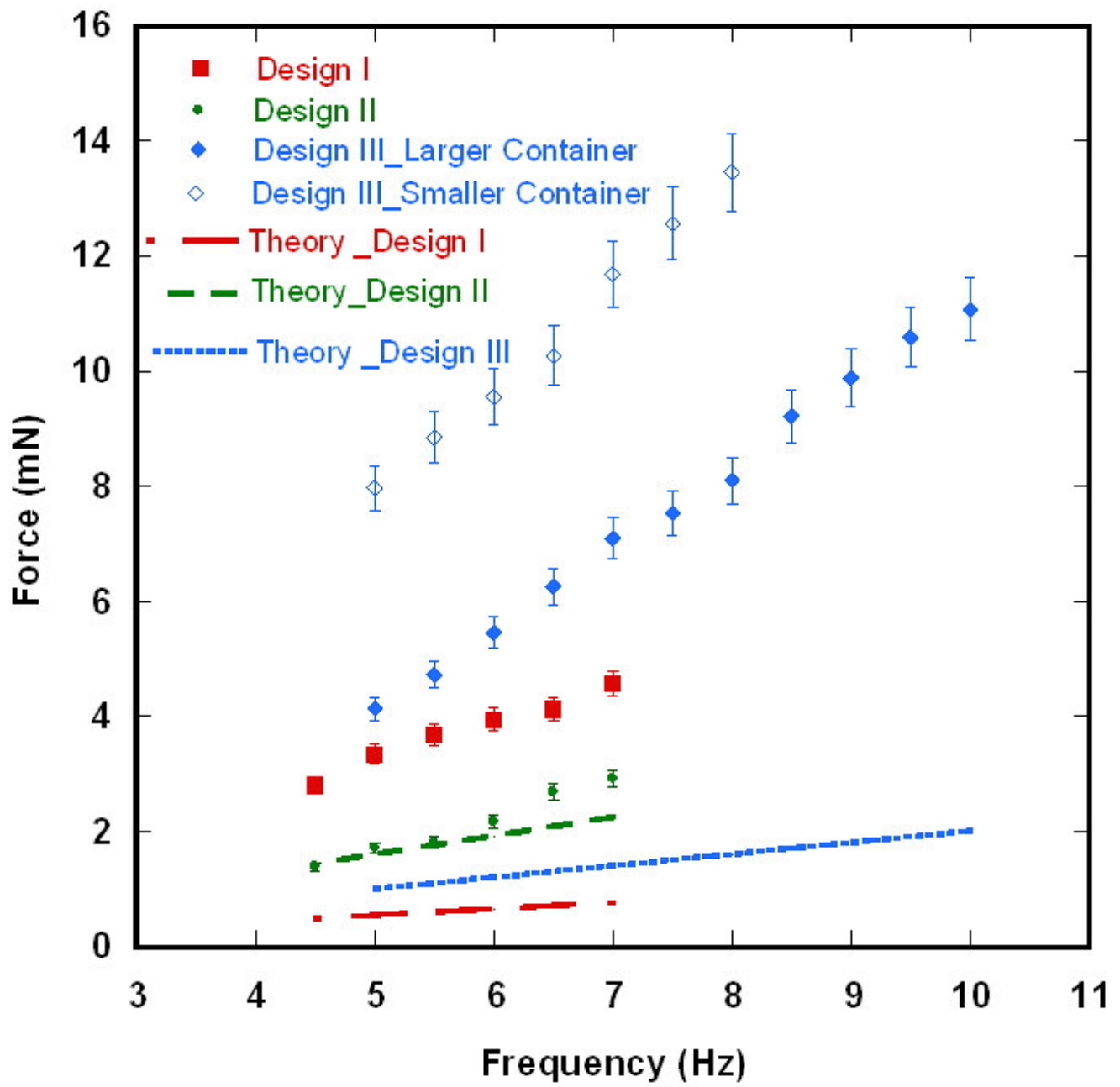












## List of Figure Captions

Fig.1. Transmission Electron Microscopy (TEM) image of *E. Coli* (x3515) "Image courtesy of Dennis Kunkel Microscopy, Inc."

Fig.2. Scanning Electron Microscopy (SEM) image of green alga (x600) "Image courtesy of Dennis Kunkel Microscopy, Inc."

Fig. 3. Schematic of the microscale swimming robot with helical wave propulsion

Fig.4. Efficiency of the helical wave propulsion as a function of non-dimensionalized geometrical parameters

Fig.5. Non-dimensionalized velocity of the robot with helical wave propulsion method as a function of non-dimensionalized geometrical parameters

Fig. 6. Schematic of the microscale swimming robot with planar wave propulsion

Fig.7. Efficiency of the planar wave propulsion as a function of non-dimensionalized geometrical parameters

Fig.8. Non-dimensionalized velocity of the robot with planar wave propulsion as a function of non-dimensionalized geometrical parameters

Fig. 9. Experimental setup for helical wave propulsive force measurement

Fig.10. Experimental result for the trust force generated by helical wave propulsion of the scaled-up prototype in silicone oil